https://doi.org/10.5194/essd-2026-300
Preprint. Discussion started: 20 May 2026

Open Access Earth System Science Data Discussions

High-resolution dataset of 2024 typhoons in the northern South China Sea captured by a collaborative network of underwater gliders and autonomous underwater vehicles

Jiawei Qi[1,3], Lei Liu[1,2], Wenhu Liu[4], Jianfang Fei[1,2], Jiancheng Yu[5], Zhanhong Ma[1,2], Zhentao Chen[1], Huabin Mao[6], Zhiduo Tan[5], Xiaogang Huang[1], Xiaoping Cheng[1]

[1]College of Meteorology and Oceanography, National University of Defense Technology, Changsha, China

[2]Key Laboratory of High Impact Weather (Special), China Meteorological Administration, Changsha, China

[3]School of Marine Science and Technology, Tianjin University, Tianjin, China

[4] Institute of Artificial Intelligence, Collaborative Innovation Center for the Marine Artificial Intelligence, Shanghai University, Shanghai, China

[5]Shenyang Institute of Automation, Chinese Academy of Sciences, Shenyang, China

[6]State Key Laboratory of Tropical Oceanography, South China Sea Institute of Oceanology, Chinese Academy of Sciences, Guangzhou, China

Correspondence: Lei Liu (liulei17anj@nudt.edu.cn); Jianfang Fei (Feijf@sina.com)

Abstract: Typhoon-induced ocean responses are not only a key mechanism for regulating global heat transport and maintaining the energy balance of the climate system, but also the core physical processes underlying the intense exchange of matter and energy at the air-sea interface under extreme dynamic forcing. However, traditional passive sampling methods are limited by their discontinuous and sparse spatiotemporal coverage, making it difficult to capture the complete three-dimensional structure and rapid evolution of upper-ocean responses during the critical window of typhoon passage. Autonomous Underwater Vehicles (AUVs) and Underwater Gliders (UGs), with their active tracking and sampling capabilities, can effectively resolve the spatiotemporal evolution of these highly dynamic processes. This paper presents a high-resolution temperature-salinity dataset covering the passage of seven typhoons in the South China

https://doi.org/10.5194/essd-2026-300
Preprint. Discussion started: 20 May 2026

Open Access Earth System Science Data Discussions

Sea during 2024. Constructed from collaborative observations by 62 UGs and 2 AUVs, the dataset achieves an average spatial resolution of 2.4–3.8 km and an average temporal resolution of 3.5–4.3 h (99.7% of the samples had resolutions within 8.4 km and 6.7 h, respectively). The dataset successfully captures the complex upper-ocean temperature and salinity responses under typhoon forcing, including cooling and salinity increase due to pumping, cooling and salinity decrease triggered by freshwater caps formed by precipitation, cooling and salinity decrease caused by background warm eddies, and significant near inertial oscillations in temperature and salinity. This dataset holds significant potential for in-depth investigation of typhoon-ocean coupling mechanisms and for improving the accuracy of numerical model forecasts.

1 Introduction

Typhoon-induced ocean responses, characterized by intense nonlinear momentum and energy exchanges, often trigger complex multiscale dynamic processes, including near inertial oscillations (NIOs), enhanced vertical mixing, and restructuring of the subsurface flow field (Liao et al., 2025; Mei et al., 2013; Mishra et al., 2026; Price, 1981; Reichl et al., 2024; Vlasova et al., 2022; Wang et al., 2022; Zhang et al., 2021). This intense dynamical coupling requires observational systems to possess high spatiotemporal synchrony and enhanced resolution capabilities to capture the transient characteristics of rapid oceanic responses during typhoon passage. Under typhoon forcing, the wind stress energy absorbed by the ocean surface primarily triggers intense vertical shear, inducing unstable turbulent mixing that draws sub-surface cold water to the surface. Concurrently, Ekman pumping driven by wind stress vorticity also generates upwelling of sub-surface cold water. The combined action of

https://doi.org/10.5194/essd-2026-300
Preprint. Discussion started: 20 May 2026


Open Access Earth System Science Data Discussions

these two processes forms a distinct cold wake structure in the upper ocean (John et al., 2025; Ye et al., 2023; Zhou et al., 2025). As one of the regions with the highest frequency of typhoon activity globally, the South China Sea's semi-enclosed topography and complex background flow field result in particularly intense and unique typhoon-ocean interactions (Guan et al., 2024; Yang et al., 2022; Zheng and Wang, 2023). These typhoon-driven vertical exchange processes and three-dimensional circulation reconstruction play a central role in oceanic energy cascading, heat redistribution, and material fluxes across isopycnal surfaces, exerting profound impacts on regional climate prediction and the evolution of marine ecosystems (Chen et al., 2026; Fan et al., 2023; Gong et al., 2026; Wada and Yanase, 2024; Yi et al., 2024; Yu et al., 2021; Zhang, 2023).

Currently, the primary observational platforms for typhoon-induced ocean responses include satellite remote sensing, moored buoy array, Argo buoy array, Lagrangian drifter, underwater glider (UG), and autonomous underwater vehicle (AUV). The extreme sea conditions triggered by typhoons make it difficult to conduct traditional ship-based oceanographic surveys. Satellite observations can only provide characteristics of sea surface changes. They cannot characterize sub-surface dynamic and thermal processes, and their insufficient temporal resolution makes it difficult to resolve high-frequency wave signals (Lu et al., 2025; Zhang et al., 2024a). Moored buoy arrays can provide long-term, continuous, fixed-

https://doi.org/10.5194/essd-2026-300
Preprint. Discussion started: 20 May 2026


Open Access Earth System Science Data Discussions

point observations and are often used to capture typhoon-induced near inertial waves, but their sparse spatial distribution necessitates "stationary" observations: if located too far from the typhoon, they cannot capture large-scale response processes (Athulya et al., 2026; Chen et al., 2025; Tang et al., 2025; Wang et al., 2021; Yang et al., 2021, 2024; Zhang et al., 2016, 2018). Argo buoy arrays and Lagrangian drifters can respectively record the three-dimensional thermodynamic structure and ocean current response induced by typhoons. However, the former's spatial and temporal resolutions of approximately 10 days and 100 km are insufficient to capture high-frequency variability, while the latter cannot obtain information on subsurface circulation. Furthermore, the uncontrollable nature of their passive drifting poses significant challenges for data collection (Chen et al., 2021; Goni et al., 2017; He et al., 2024a, b; Li et al., 2022, 2021; Liu et al., 2026; Qiu et al., 2025; Ruan et al., 2024; Sala et al., 2024; Tian and He, 2025; Trenggono et al., 2024; Wang et al., 2022).

Attributed to their active observation capabilities, UGs and AUVs have become essential tools for exploring the marine environment over the past two decades (Qiu et al., 2025). These platforms offer advantages such as low cost, long endurance, high controllability, and reusability. Both platforms are equipped with conductivity-temperature-depth (CTD) sensors to simultaneously acquire vertical temperature and salinity profiles, enabling the successful detection of dynamic features such as the warming

https://doi.org/10.5194/essd-2026-300
Preprint. Discussion started: 20 May 2026

trend of the Gulf Stream (Todd and Ren, 2023) and water mass exchange between the Bay of Bengal and the Arabian Sea (Rainville et al., 2022). Previously, Qiu et al. (2025) successfully acquired high spatiotemporal resolution datasets by coordinating the deployment of UGs and AUVs across mesoscale eddy regions, conducting systematic observations primarily focused on mesoscale eddies and their associated submesoscale processes. Recently, Zhang et al. (2024b) further utilized an unmanned observation array comprising UGs and wave gliders to conduct collaborative observations of Typhoon Koinu (2023), successfully revealing the evolution of the air-sea environment within the typhoon's core region. Furthermore, the "Yunfan" hybrid wind-wave-powered unmanned vessel, developed by Tian et al. (Huang, 2025), successfully completed close-range observations of the core region of Typhoon Wutip, transmitting key meteorological parameters such as wind speed and air pressure in real time. Although the aforementioned studies have made significant progress in using unmanned platforms to observe typhoons, to date, there have been no reports of publicly released datasets derived from observations of typhoon-induced oceanic responses using platforms with active observation capabilities. Therefore, this study designed an experiment specifically for observing typhoon-induced ocean responses and successfully conducted comprehensive field observations in the South China Sea from late May to early December 2024. This paper presents a

https://doi.org/10.5194/essd-2026-300
Preprint. Discussion started: 20 May 2026


Open Access Earth System Science Data Discussions

dataset of typhoon-induced oceanic temperature and salinity responses obtained from the experiment, aiming to demonstrate and validate the unique advantages and robust capabilities of UGs and AUVs in resolving oceanic dynamic processes under typhoon forcing.

2 Datasets

2.1 UG and AUV experiment sites

The experimental design of this study aims to systematically characterize the dynamic response of the upper ocean to typhoon forcing. The observation platform consists of the "SeaWing" series of UG (Yu et al., 2011), independently developed in China, and "SeaWhale" AUV. Field observations commenced in late May 2024 and concluded in early Dec. 2024, spanning approximately six months. During this period, a total of 62 UGs and 2 AUVs were deployed, accumulating over 57,000 water temperature and salinity profile data points. A total of seven typhoon events were recorded during the observation window. Through spatiotemporal matching analysis, 112 valid paired samples were established between typhoon events and UG/AUV observation data, totaling 4,459 temperature-salinity profiles. Fig. 1 shows the tracks of the UGs and AUVs. Tab. 1 details the deployment parameters for each platform, including operational periods, sensor types carried, and maximum diving depths. Additionally, complete mission metadata has been archived in NetCDF (.nc) format (Qi et al., 2026).

https://doi.org/10.5194/essd-2026-300
Preprint. Discussion started: 20 May 2026

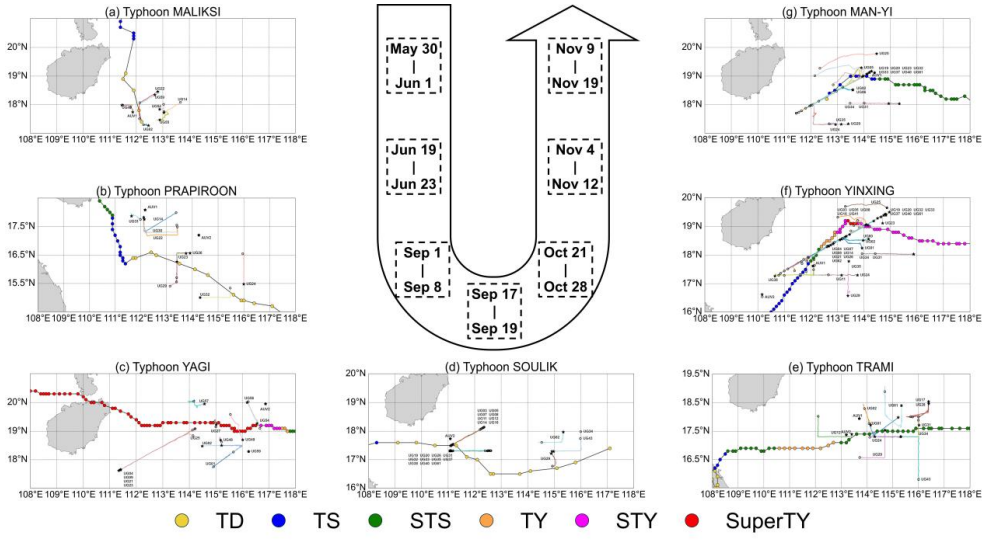

Figure 1. Trajectory of the 7 typhoons and the UGs/AUVs. These 7 typhoons are listed in numerical order: MALIKSI (No. 2402), PRAPIROON (No. 2404), YAGI (No. 2411), SOULIK (No. 2415), TRAMI (No. 2420), YINXING (No. 2422), and MAN-YI (No. 2424). The legend indicates typhoon intensity, and the dotted lines with intensity markers represent the typhoon paths. The text labels "UG" and "AUV" are placed near their respective tracks, and the "★"represents the starting point, and the "○" represents the endpoint.

2.2 Statistics of UG and AUV resolutions

During the operational period, the observation area experienced a total of 8 typical typhoon events (Fig. 1 and Tab. 1, "TY event" column), which were primarily concentrated between Sept. and Nov., exhibiting a pattern of higher frequency in the autumn. Among these, the joint observation network comprising UGs and AUVs successfully captured 7 typhoon events; only Typhoon TORAJI was not effectively observed because it was located at the edge of the observation network. Given that the deployment

https://doi.org/10.5194/essd-2026-300
Preprint. Discussion started: 20 May 2026


Open Access Earth System Science Data Discussions

density of UGs was significantly higher than that of AUVs, we established differentiated spatiotemporal matching thresholds during the process of aligning observation profiles with typhoon tracks. We used thresholds to filter the entry locations and times for UGs and AUVs, the spatiotemporal matching threshold for UGs was set to ≤(3 h, 100 km), while a more lenient threshold of ≤(3 h, 150 km) was applied to AUVs. Statistical analysis shows that during each typhoon passage, the maximum navigation distance of the observation platforms exceeded 120 km (Tab. 1, "Max. trajectory length" column), fully covering the typhoon passage period and achieving forward deviation (Tab. 1, "Equip. Active Days" column, extending 2 days before and after the passage), ensuring effective observation of typhoon-induced oceanic responses.

A statistical analysis of the spatiotemporal sampling characteristics of UGs and AUVs during typhoons was conducted. Fig. 2a and Fig. 2b show the mean and standard deviation of the operational distance and duration of the observation network during typhoons. The results indicate that navigation activities primarily occurred at a spatial resolution of 2.4–3.8 km and a temporal resolution of 3.5–4.3 h. According to the 3σ principle, 99.7% of the data fell within 8.4 km and 6.7 h. Fig. 2c presents box plots of the navigation distance and duration for a single operational cycle of the observation platforms. As shown in the figure, the median navigation distance for the devices during the seven typhoons mostly ranged between

https://doi.org/10.5194/essd-2026-300
Preprint. Discussion started: 20 May 2026

2 and 4 km. The steel-blue rectangular blocks representing the Interquartile Range (IQR) generally have a wide height, indicating a high degree of dispersion in navigation distance. Fig. 2d shows a box plot of the navigation time for a single operational cycle of the observation platform, indicating that the median navigation time is concentrated around 4 hours. Except for Typhoons MALIKSI and MAN-YI, where the IQR (represented by the sea-green rectangular blocks) is relatively wide, the IQR for the remaining typhoons is generally narrow. This suggests that over 50% of the observation duration is highly concentrated within 4 h, reflecting the relative stability of the temporal sampling.

It is worth noting that there are some outliers in the navigation distance box plot (Fig. 2c): these include the red dots above the boxes for Typhoons PRAPIROON, YAGI, and SOULIK, with maximum navigation distances reaching as far as 17 km; as well as a small number of outliers with extremely short distances below the PRAPIROON and SOULIK boxes (some less than 1 km). Similarly, the navigation time box plot (Fig. 2d) also contains a certain number of outliers (such as the red dots on both sides of the boxes for YAGI, SOULIK, and TRAMI). These outliers are not merely data noise, but reflect the “relatively controlled in time and random in space” movement characteristics of the observation equipment during typhoons, and may be a direct record of the interaction between the observation platform and the complex oceanic dynamic environment

https://doi.org/10.5194/essd-2026-300
Preprint. Discussion started: 20 May 2026


Open Access Earth System Science Data Discussions

induced by typhoons. The outliers on the navigation distance box plot may reflect the violent changes in the typhoon-induced flow field, embodying the nonlinear superposition effect of the observation platform's own navigation speed and the typhoon-induced flow field moving with or against the current. Meanwhile, the outliers on the navigation time box plot may stem from abnormal operational cycles caused by communication disruptions, protective mechanisms such as deep-diving to avoid currents, or adaptive attitude adjustments under extreme sea conditions.

The analysis of the spatiotemporal characteristics described above indicates that the dataset obtained through the combined observations of UGs and AUVs not only has the capability to resolve typhoon-induced mesoscale (50–300 km) oceanic dynamic processes but also possesses sufficient spatiotemporal resolution to capture high-frequency (characteristic timescale > 2*4 h, such as near inertial oscillations) dynamic processes, thereby providing high-quality data support for a deeper understanding of the typhoon-ocean interaction mechanisms.

https://doi.org/10.5194/essd-2026-300
Preprint. Discussion started: 20 May 2026

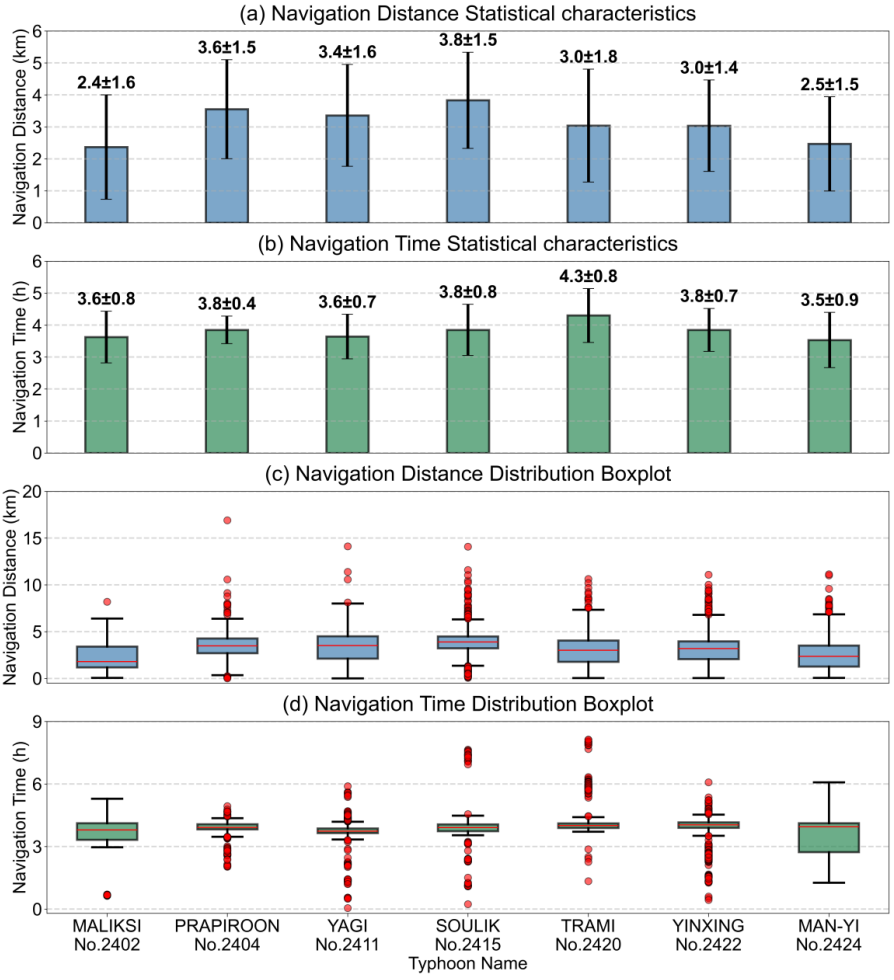

Figure 2. Statistics on spatial and temporal sampling. (a) and (b) show the mean and standard deviation of the normal distributions of spatial and temporal sampling, respectively; the bars represent the mean, and the black lines represent one standard deviation. (c) and (d) show box-and-whisker plots of the spatial and temporal samples. The red horizontal line represents the median of the sample. The height of the box is the difference between the 75th and 25th percentiles of the data, known as the interquartile range, which encompasses 50% of the sample. The black whiskers indicate the range of variation in the sample, and the red circles mark outliers.

228 Table 1. Available datasets from UGs and AUVs.

No.	TY event	Equip. Active Days (2 days pre- and post-TY passage)	No. of matches (unit) UG/AUV	No. of profiles (profile) UG/AUV	Min. distance to TY center (km)	Max. trajectory length (km)	Avg. daily profiles (profile)	Avg. profiles per Equip. during TY (profiles)
1	MALIKSI	28 May-3 Jun 2024, 7 d	7/1	302/3	24.7	128.49	43	43
2	PRAPIROON	17 Jul-25 Jul 2024, 9 d	9/2	440/2	16.3	140.12	48	48
3	YAGI	30 Aug-10 Sept 2024, 12 d	14/1	964/1	7.6	**336.65**	80	68
4	SOULIK	15 Sept-21 Sept 2024, 7 d	23/1	921/1	26.0	161.94	131	40
5	TRAMI	19 Oct-30 Oct 2024, 12 d	11/2	695/2	9.8	182.72	57	63
6	YINXING	2 Nov-14 Nov 2024, 13 d	**31/2**	**2267/3**	**3.9**	297.23	**174**	73
7	MAN-YI	7 Nov-21 Nov 2024, 15 d	17/1	1515/1	12.7	299.56	101	**89**
	Average	≈10.7 d	≈16/1	≈637/2	—	—	≈90	≈60
	Total	75 d	112/10	4459/13	—	—	—	—

229 TY: typhoon; UG: underwater glider; AUV: autonomous underwater vehicle; Equip.: equipment.

230

https://doi.org/10.5194/essd-2026-300
Preprint. Discussion started: 20 May 2026

2.3 Sampling Performance of the Observation Network During Typhoons

During typhoon passages, strong winds and intense oceanic disturbances posed significant challenges to glider observation operations. Among the seven typhoon events covered in this study, a total of 112 valid "typhoon-UGs/AUVs" matching records were obtained, involving 62 UGs and 2 AUVs. It is worth noting that while the vast majority of UGs participated in typhoon observations within the study area, the deployment density of AUVs was relatively low, with no more than three matching records generated per typhoon event.

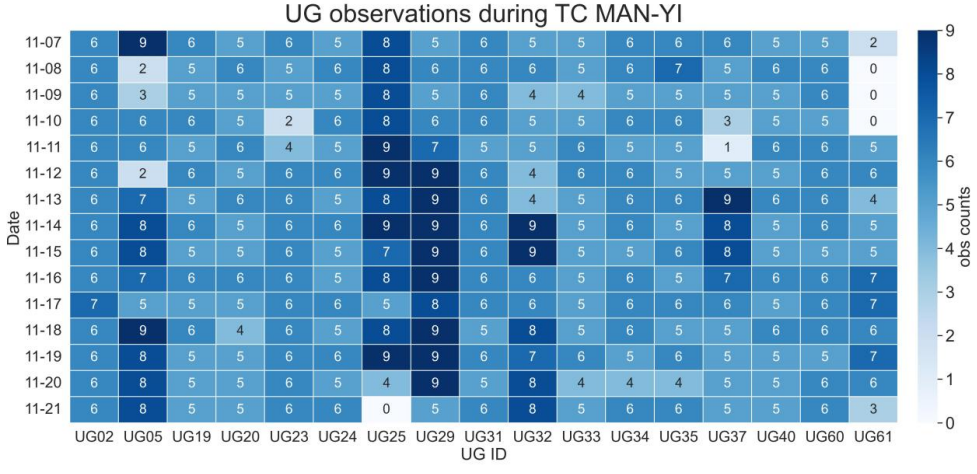

Figure 3. Heatmap of UG data collection during Typhoon MAN-YI. The x-axis shows the device IDs that detected MAN-YI, the y-axis shows the observation time, and the number of cells represents the number of temperature-salinity profiles.

Statistical results show that, except for Typhoon MALIKSI (No. 2402), all other typhoons were detected by at least 10 observation devices. Among them, Typhoon SOULIK (No. 2415) and Typhoon YINXING (No. 2422) were detected by 24 and 33 observation devices, respectively ("No.

https://doi.org/10.5194/essd-2026-300
Preprint. Discussion started: 20 May 2026


Open Access Earth System Science Data Discussions

of matches" column in Table 2). Taking the UGs observing MAN-YI (No. 2424) as an example, a total of 17 UGs recorded this typhoon event (see Fig. 3). During this event, the maximum number of UG observations recorded in a single day reached 110 (Nov. 14), with a daily average of no less than 97; the maximum number of records from a single device during the typhoon event was 114 (UG29), and the average number of records from a single device was no less than 86.

A statistical analysis of all observation pairs revealed the following: (1) In terms of temporal coverage, the average observation duration per pair was approximately 10.7 days, providing complete coverage of the pre-typhoon background conditions, the typhoon forcing process, and the post-event recovery phase. (2) In terms of spatial coverage, the average track length per mission was 153.24 km, with a cumulative total track length of 17,162.69 km, demonstrating the UG's effective observational capability over a large oceanic area during typhoon events. More importantly, all pairs included at least one observation profile within 100 km of the typhoon center, and approximately 17.2% of the pairs included profiles within the 25-km near-field range, indicating that some UGs were able to directly observe air-sea interaction processes in the typhoon's core region.

Overall, UG offers significant spatiotemporal advantages in typhoon observations. On the one hand, UG is capable of maintaining continuous and stable observations throughout a typhoon event, providing a complete

https://doi.org/10.5194/essd-2026-300
Preprint. Discussion started: 20 May 2026

data chain for the study of typhoon-driven ocean response processes. On the other hand, the combination of far-field and near-field observational data allows research to simultaneously reveal the forcing mechanisms in the typhoon's core and the response propagation effects in the outer regions. In summary, UG observations not only demonstrate the comprehensiveness of typhoon event monitoring in terms of sample size and coverage but also maintain reliability under extreme near-field conditions, providing a solid data foundation for understanding the oceanic dynamical and thermal responses during typhoon events.

3 Data quality control method

Before investigating the response of the upper ocean to typhoon processes, we performed rigorous quality control and thermal lag correction on the UG and AUV datasets.

3.1 Data quality control

This study employs the "Sea-Wing" UG and 'SeaWhale' AUV as core observation platforms. The "Sea-Wing" integrates multi-source communication and navigation subsystems, including Iridium communication, wireless telemetry modules, high-precision attitude sensors, Global Positioning System receivers, pressure sensors, and obstacle-avoidance sonar. Meanwhile, the "SeaWhale" integrates a CTD sensor, a Doppler current profiler, obstacle-avoidance sonar, and a propulsion module. It can perform zigzag profiling maneuvers like a glider

https://doi.org/10.5194/essd-2026-300
Preprint. Discussion started: 20 May 2026

as well as cruising at a fixed depth. Oceanographic parameters are collected at 6-second intervals via a non-pumped CTD sensor. Before analyzing ocean phenomena, all raw data undergo rigorous quality control (QC) and strictly adhere to Integrated Ocean Observing System (IOOS) standards. Table 2 details the 13-step systematic QC process tailored to the specific characteristics of glider data, along with the corresponding decision logic.

This quality control protocol effectively eliminates significant errors caused by positioning drift, sensor failure, and non-physical abrupt changes, significantly improving the spatiotemporal continuity and physical consistency of the data. However, this process cannot resolve the systematic thermal lag bias caused by mismatched response times between the temperature and conductivity sensors in non-pumped CTDs. Such errors often produce spurious salinity peaks, particularly when the glider traverses strong thermoclines. Therefore, specialized corrections for sensor dynamics are required. Section 3.2 details the physical mechanisms of thermal lag effects and introduces a correction algorithm optimized for variable flow rates to further eliminate residual systematic synchronization errors.

311 Table 2. QC Protocol Steps for UG and AUV Data

No.	Test item	Purpose	No.	Test item	Purpose
1	Time/Gap	Remove invalid timestamps; fix abnormal gaps.	8	Spike	Eliminate abrupt noise using depth-dependent thresholds.
2	Location	Discard coordinates outside operational boundaries.	9	Rate of Change	Filter fluctuations exceeding local physical limits.
3	Position on Land	Remove points erroneously located on land.	10	Frozen Value	Delete sequences of constant sensor readings.
4	Displacement	Discard data with anomalous positioning drift.	11	Vertical Velocity	Remove profiles with stalled or unrealistic speeds.
5	Pressure	Sort profiles; fix depth inversions and duplicates.	12	Density Inversion	Flag layers violate hydrostatic stability.
6	Gross Range	Filter values beyond global/regional physical limits.	13	Mixed Layer Disc.	Remove non-physical jumps near mixed layer depth.
7	Climatology	Discard outliers deviating from historical means.			

312

https://doi.org/10.5194/essd-2026-300
Preprint. Discussion started: 20 May 2026

3.2 Thermal lag correction

When UGs and AUVs are equipped with pump-less CTD sensors for observations, a phenomenon known as the “thermal lag effect” occurs due to the spatial separation and differences in response time between the temperature sensor (typically located outside the conductivity measurement chamber) and the conductivity sensor (located inside the measurement chamber). This effect is particularly pronounced when traversing regions with steep temperature gradients, such as the thermocline, leading to systematic biases in derived salinity data and the generation of spurious salinity peaks. Furthermore, the unstable operating speeds of these platforms cause dynamic changes in the seawater flow rate through the conductivity cell, thereby complicating the calibration process. To address this challenge, calibration methods initially developed for ship-based CTDs laid the foundation for data processing on mobile platforms. Morison et al. (1994) pioneered an empirical method based on minimizing the deviation in the temperature-salinity (T-S) relationship, estimating the lag parameter by constraining the salinity difference between the up- and down-trajectory profiles. Building on this, Garau et al. (2011) proposed an optimization method for pump-less gliders, employing a sequential quadratic programming (SQP) algorithm to minimize the enclosed area between the up- and down-trending T-S curves, thereby obtaining optimal correction parameters. Liu et al. (2015) further refined the correction

https://doi.org/10.5194/essd-2026-300
Preprint. Discussion started: 20 May 2026

strategy for regions with strong thermoclines, effectively mitigating salinity abrupt changes under steep gradients.

To eliminate salinity errors caused by thermal lag, this study employs a synchronous conductivity correction method, which mathematically reconstructs conductivity data to match the response characteristics of the temperature sensor. The discrete recursive formula for conductivity correction is expressed as:

$$C_T(n) = -bC_T(n-1) + \gamma a\left[T(n) - T(n-1)\right] \quad (1)$$

Where C_T denotes the corrected actual conductivity at the n-th sampling instant (corresponding to the temperature sensor location), $T(n)$ is the measured temperature, and γ is the sensitivity coefficient of conductivity to temperature. The coefficients a and b are determined by the following equations:

$$a = 4f_n \cdot \alpha\tau\left(1 + 4f_n \cdot \alpha\tau\right)^{-1}, b = 1 - 2a\alpha^{-1} \quad (2)$$

Where f_n is the Nyquist frequency, α is the dimensionless correction amplitude, and τ is the time constant (in seconds). The parameters α and τ are critical determinants of correction accuracy, and their values typically depend on the velocity of seawater flowing through the conductivity cell. Given that the flow velocity for UGs and AUVs varies dynamically during diving and ascending phases, this study employs a variable-flow coefficient method, modeling α and τ as functions of the flow velocity V:

https://doi.org/10.5194/essd-2026-300
Preprint. Discussion started: 20 May 2026

$$\alpha(n) = \alpha_o + \alpha_s V(n)^{-1}, \tau(n) = \tau_o + \tau_s V_f(n)^{-0.5} \quad (3)$$

Where $V(n)$ represents the average flow velocity of seawater through the conductivity cell at the n-th instant (m/s); the subscripts O and S denote the offset and slope, respectively; and $\alpha_o, \alpha_s, \tau_o, \tau_s$ are the characteristic parameters to be fitted.

In the data processing workflow of this study, we first adopted the SQP optimization framework proposed by Garau et al. (2011). Assuming that the properties of the water mass remain constant during a single profile ascent and descent, we iteratively solved for the characteristic parameters by minimizing the difference in area between the ascent and descent T-S curves. After completing this preliminary thermal lag correction and calculating salinity over the standard atmospheric pressure layer, we incorporated the improved strategy proposed by Liu et al. (2015) to further eliminate residual salinity jump noise caused by sensor response mismatches. Specifically, we applied median filtering to the corrected temperature, conductivity, and salinity time series to ensure the reliability and smoothness of the final dataset.

3.3 Cross-validation results

To assess the reliability of the data, the temperature and salinity profiles observed by the UG were cross-validated against ship-based CTD measurements collected in July 2024 (Fig. 4A(a)-4A(c)). These CTD profile data were obtained using the SBE 911plus CTD instrument, which

https://doi.org/10.5194/essd-2026-300
Preprint. Discussion started: 20 May 2026

collects data at a high frequency of 24 Hz and has an operational range exceeding 1,000 m in depth, which exceeds the maximum operational depth of the gliders. Prior to deployment, the SBE 911plus CTD sensors underwent a rigorous standard calibration process to ensure the reliability of the observational data. Given the sparse distribution of AUV observation stations (Fig. 1) and the significant spatial gaps between AUV tracks and ship-based CTD deployment points, a direct comparison was not feasible. Therefore, spatially and temporally adjacent UG profiles were used as a reference benchmark to indirectly validate the AUV temperature and salinity profiles (Fig. 4B(a)-4B(c), 4C(a)-4C(c)).

Quantitative analysis revealed a mean bias of 0.03°C for temperature and 0.01 psu for salinity. Cross-validation among the ship-based CTD, UG, and AUV datasets indicated a high degree of consistency in the vertical hydrographic structure, thereby strongly confirming the reliability and accuracy of the multi-platform observational data used in this study.

https://doi.org/10.5194/essd-2026-300
Preprint. Discussion started: 20 May 2026

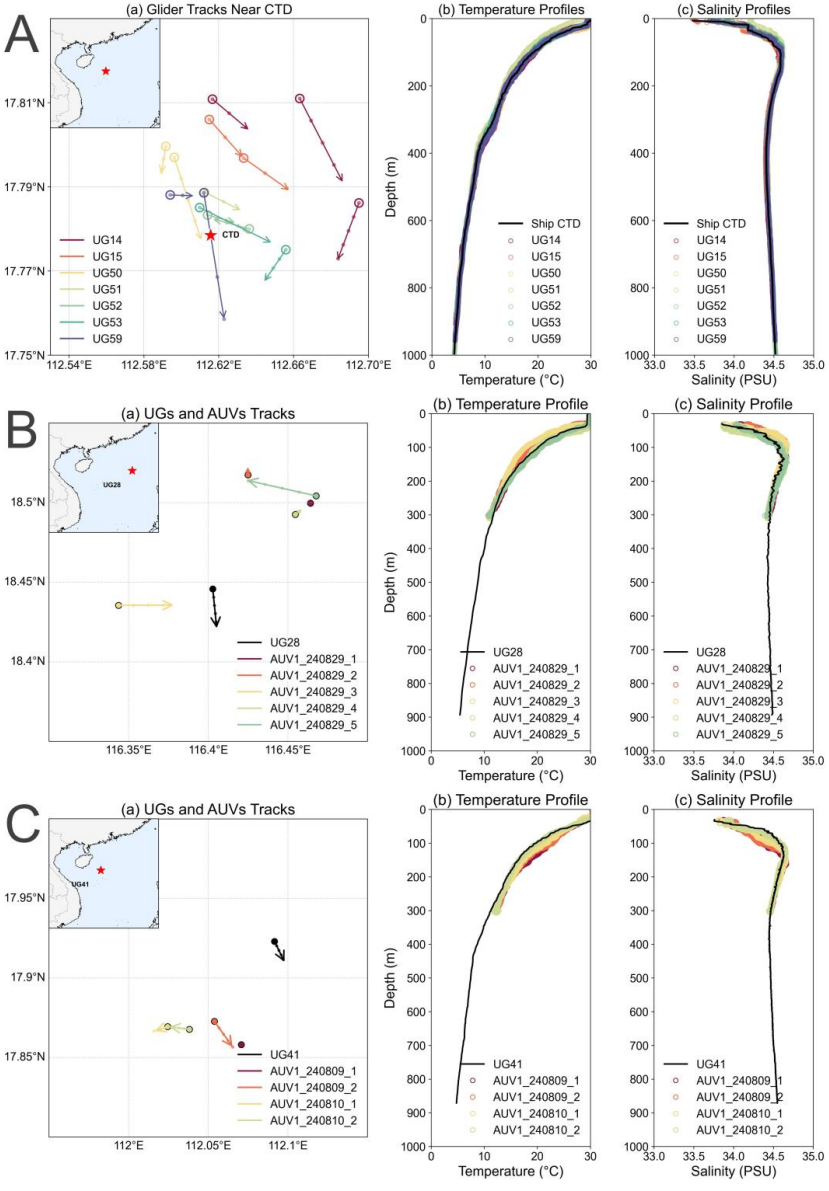

Figure 4. Cross-validation of co-located observations from shipboard, UG-mounted, and AUV-based CTDs, focusing on: A(a)-C(a) spatial correspondence, A(b)-C(b) temperature, and A(c)-C(c) salinity. The black lines in A(b)-A(c) represent ship-based measurements, while the black lines in B(b)-B(c) and C(b)-C(c) represent UG measurements. The colored circles represent different missions of the UG or AUV, respectively.

https://doi.org/10.5194/essd-2026-300
Preprint. Discussion started: 20 May 2026

4 The typhoon events observed by UG and AUV

4.1 Vertical variations in temperature and salinity sections observed by UGs and AUVs

Typhoons induce intense disturbances in the ocean surface layer through strong wind stresses, typically leading to a series of changes in the temperature, salinity, and depth of the mixed layer. By sailing along paths near typhoon tracks, a three-dimensional observation network comprising UG arrays and AUVs recorded hundreds of vertical temperature-salinity profiles driven by seven typhoons. Fig. 5 illustrates the thermohaline changes during the passage of three typhoons: MALIKSI (No. 2402), SOULIK (No. 2415), and MAN-YI (No. 2424).

Typically, typhoons induce significant sea surface cooling and salinity increase through intense vertical mixing driven by wind stress, Ekman pumping, and heat and freshwater flux exchanges between the ocean and atmosphere. These processes trigger the upwelling of deep cold water and the entrainment of high-salinity subsurface water, while the input of large amounts of turbulent kinetic energy disrupts stratification, leading to a deepening of the mixed layer. During the passage of Typhoon MAN-YI (No. 2424), distinct signals of sea surface cooling and salinity increase were observed in the temperature-salinity profiles (indicated by the red dashed boxes in Fig. 5C(b) and (c)). Further statistical analysis of the temperature-salinity profiles revealed that Typhoons YAGI (No. 2411),

https://doi.org/10.5194/essd-2026-300
Preprint. Discussion started: 20 May 2026

TRAMI (No. 2420), YINXING (No. 2422), and MAN-YI (No. 2424) had particularly significant cooling effects on the sea surface. Within the top 40 meters, temperatures decreased by 1–4°C, and salinity increased by 0.1–0.5 psu. Additionally, these four typhoons triggered intense vertical mixing, resulting in varying degrees of deepening of the mixing layer. Notably, following the passage of Typhoon YAGI (No. 2411), the mixing layer depth extended to approximately 80 m. In contrast, due to the observation points distance from the storm center, no significant changes in the vertical temperature-salinity structure were observed during the passage of Typhoon PRAPIROON (No. 2404).

The observation network also revealed distinctly different vertical thermohaline evolution processes during the passages of Typhoons MALIKSI and SOULIK. For Typhoon MALIKSI (No. 2402), although temperature section data recorded a brief cooling of the sea surface during the event, this was followed by significant surface warming and a sharp drop in salinity (indicated by the red dashed boxes in Fig. 5A(b) and (c)). A combined analysis of vorticity and precipitation (Appendix A Fig. A1) indicates that a strong “precipitation-radiation” coupling effect overrode the conventional wind-driven mixing cooling mechanism. Intense typhoon rainfall formed a thick, low-salinity freshwater cap at the surface (with cumulative precipitation reaching 136 mm within 24 hours after 12:00 on May 30), significantly enhancing density stratification and creating a

https://doi.org/10.5194/essd-2026-300
Preprint. Discussion started: 20 May 2026

barrier layer that effectively suppressed the upwelling and entrainment of deep cold water. Subsequently, high-intensity seasonal shortwave solar radiation rapidly heated this layer, leading to heat accumulation rather than downward diffusion, and ultimately resulting in a surface warming and precipitation-dominated salinity anomaly. In contrast, Typhoon SOULIK (No. 2415) exhibited more complex dynamical processes as it passed over the observation site (indicated by the red dashed boxes in Fig. 5B(b) and (c)). Although a typical sea-surface cooling event occurred on Sept. 19, salinity exhibited a non-monotonic "first-decrease-then-increase" pattern inconsistent with a simple cold-water upwelling mechanism. Observation trajectory and eddy field analysis confirmed that UG entered a background warm eddy between Sept. 19 and 22 (Appendix A Fig. A2). The nonlinear interaction between typhoon-induced vertical mixing and the warm eddy's inherent high-temperature, low-salinity characteristics led to the observed simultaneous initial decrease in temperature and salinity, which subsequently shifted to a cooling and salinity-increasing process due to cold water upwelling. This highlights the key moderating role of background mesoscale vortices in typhoon-induced oceanic responses.

In summary, the collaborative observation network comprising the UG array and AUVs demonstrated exceptional capability in capturing the complex oceanic responses triggered by typhoons. In addition to clearly documenting typical wind-driven mixing, cooling, and salinity increase

https://doi.org/10.5194/essd-2026-300
Preprint. Discussion started: 20 May 2026

processes, the system, leveraging its high spatiotemporal resolution, successfully captured fine-scale vertical structural changes that differ markedly from traditional wind-driven mixing mechanisms. These changes specifically include the rapid surface warming and salinity dilution triggered by Typhoon MALIKSI (No. 2402), as well as the complex temperature-salinity signals resulting from the nonlinear interaction between Typhoon SOULIK (No. 2415) and the background warm eddy. These observational results conclusively demonstrate that the UG-AUV joint observation system can accurately resolve three-dimensional temperature and salinity evolution regulated by multiple physical mechanisms under extreme weather conditions, providing critical data support for elucidating the underlying dynamics of typhoon-ocean interactions.

https://doi.org/10.5194/essd-2026-300
Preprint. Discussion started: 20 May 2026

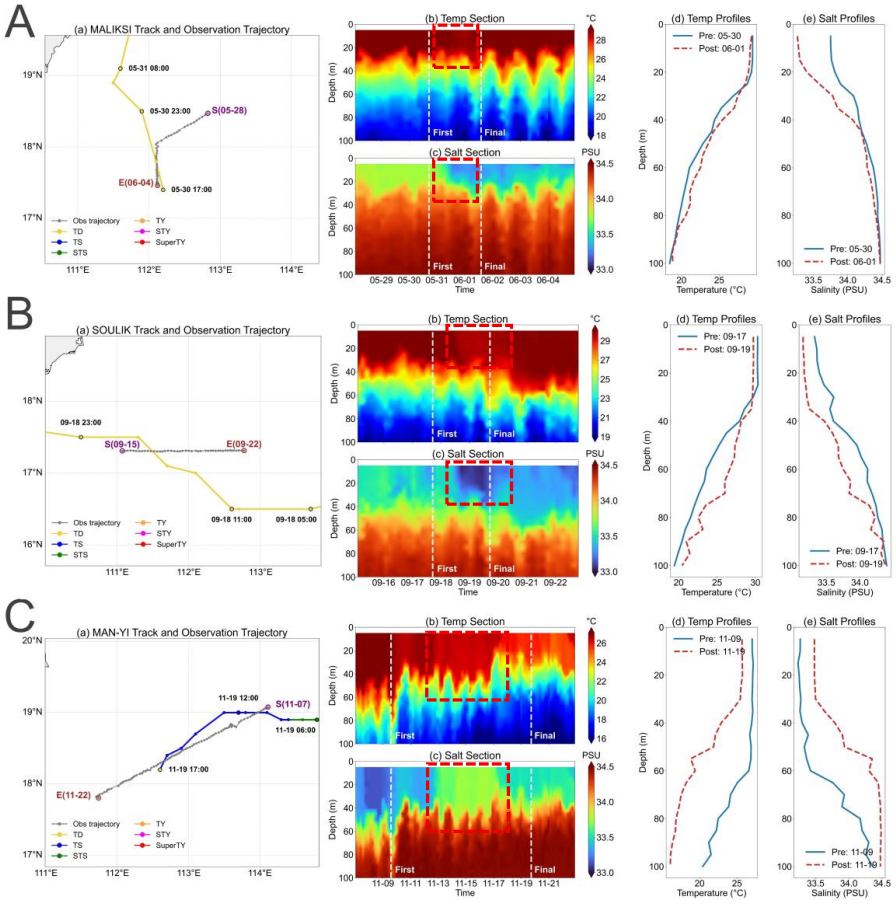

Figure 5. Typhoon-induced changes in the vertical structure of temperature and salinity (A-C show observations during Typhoons MALIKSI, SOULIK, and MAN-YI, respectively). A(a)-C(a) illustrates the relative spatial positions of the typhoon tracks and the observation platforms, while A(b)-C(b) and A(c)-C(c) show the temperature and salinity sections, and A(d)-C(d) and A(e)-C(e) show their profiles within the upper 100 m, respectively. The red dashed boxes in A(b) and A(c) show the cooling and salinity-decreasing process caused by precipitation; the red dashed boxes in A(b) and A(c) show the cooling and salinity-decreasing process caused by a background warm eddy; and the red dashed boxes in A(b) and A(c) show the cooling and salinity-increasing process caused by upwelling and vertical mixing.

4.2 Thermohaline NIOs observed by UGs and AUVs

https://doi.org/10.5194/essd-2026-300
Preprint. Discussion started: 20 May 2026


Open Access Earth System Science Data Discussions

In addition to significant thermohaline thermodynamic changes, the response of the upper ocean to typhoons is also manifested dynamically in the form of NIOs. During the mission, UGs and AUVs deployed around the typhoon tracks extensively observed typhoon-induced periodic temperature and salinity oscillations. Taking Typhoons YAGI (No. 2411), SOULIK (No. 2415), and TRAMI (No. 2420) as examples, the average latitude of the observation points during the typhoon transit was used as the reference latitude for calculating the local inertial frequency. The inertial frequency is calculated using the following formula:

$$f = 2\Omega \sin\phi \tag{4}$$

where f is the local inertial frequency, Ω is the Earth's rotation rate (a constant), and ϕ is the local latitude. Based on the local inertial frequency, a fourth-order Butterworth filter was applied to extract the NIO components of temperature and salinity from the section data, using a filtering frequency band of $[0.8,1.2]\,f$.

https://doi.org/10.5194/essd-2026-300
Preprint. Discussion started: 20 May 2026

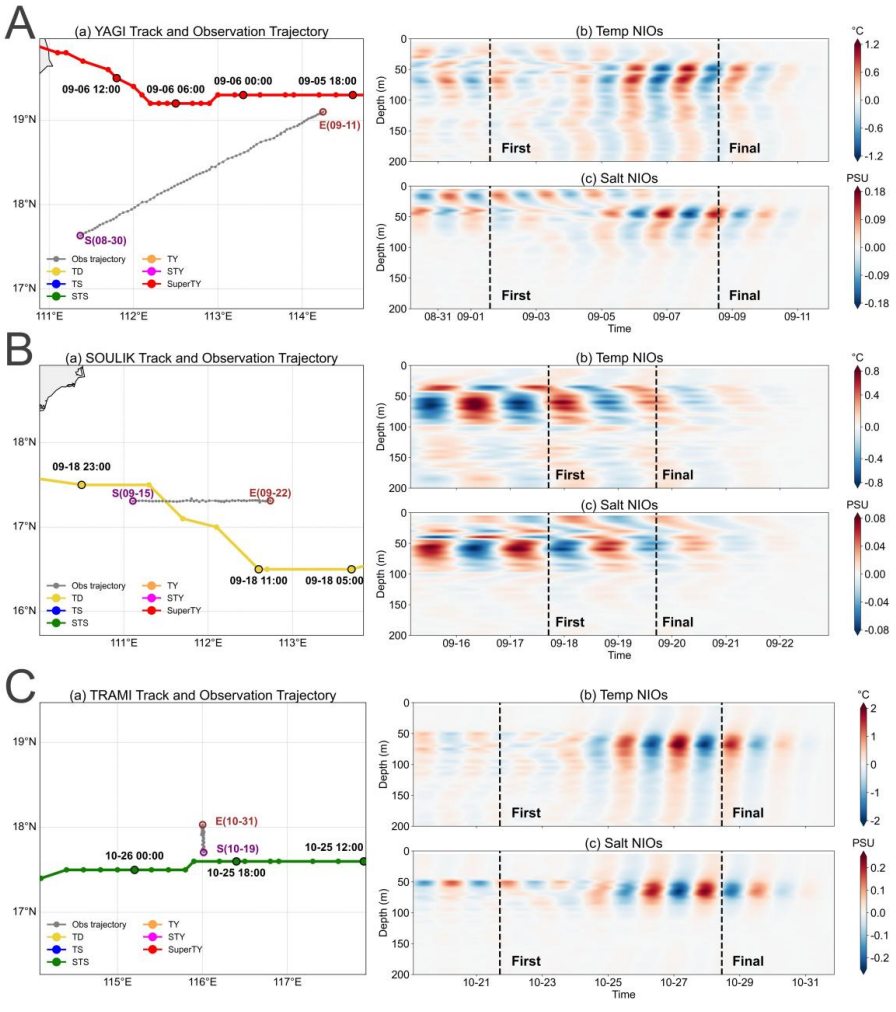

Figure 6. Observations of NIOs during Typhoons (A) YAGI, (B) SOULIK, and (C) TRAMI. Panels (a) depict typhoon tracks and observational trajectories; (b) temperature NIOs; and (c) salinity NIOs. In panel (a), colored lines indicate typhoon tracks with intensity information, where specific points highlighted by black outlines denote the time of passage. Gray lines represent the trajectories of the UG or AUV, with the start (purple circle, labeled "S(month–date)") and end (brown circle, labeled "E(month–date)") points emphasized. In panels (b) and (c), vertical black dashed lines mark the times of the first and final typhoon warnings, labeled "First" and "Final," respectively.

https://doi.org/10.5194/essd-2026-300
Preprint. Discussion started: 20 May 2026


Open Access Earth System Science Data Discussions

Observational results from systems deployed in the vicinity of the typhoon-affected regions of YAGI, SOULIK, and TRAMI indicate that significant periodic variations in the upper-ocean temperature and salinity structure occurred after the passage of the typhoons. As shown in the series of panels in Fig. 6(b) and (c), temperature-induced NIOs were primarily confined to the upper 200 m of the water column, whereas salinity NIOs exhibited a notably shallower influence depth, mainly concentrated within the upper 100 m. In this study, the 75 m depth layer was selected, where NIOs signals were particularly strong, to compute the power spectral density and oscillation periods of temperature and salinity NIOs (Appendix A Fig. A3). The results show that the observed NIO oscillation periods closely match the local inertial period. Specifically, the NIO frequency derived from Typhoon TRAMI (0.0260 cph) deviates by only 1% from the local inertial frequency (0.0257 cph), and the calculated oscillation period (38.5 h) differs from the inertial period (38.9 h) by merely 0.4 h.

Statistical analysis of NIOs data of 7 typhoons reveals that the mean period of temperature NIOs is 39.08 ± 3.86 h, while that of salinity NIOs is 38.54 ± 3.52 h. Both are clustered around 39 h, which is consistent with the theoretical inertial period (~39 h) at the observational network's operational latitude (~18°N). The mean amplitude of temperature NIOs is 2.0 °C, and that of salinity NIOs is 0.16 PSU, both falling within the typical range for near-inertial oscillations in temperature and salinity. The high

https://doi.org/10.5194/essd-2026-300
Preprint. Discussion started: 20 May 2026

539 degree of consistency between the oscillation periods of temperature and
540 salinity NIOs indicates that they reflect the same underlying physical
541 process—namely, typhoon-induced near-inertial oscillations in the upper
542 ocean.

543 In summary, the UG and AUV systems deployed during this
544 observational campaign successfully captured temperature and salinity
545 NIO signals in the upper ocean following typhoon passage, owing to their
546 capability for large-scale, high-precision, and continuous monitoring.
547 These instruments clearly revealed the vertical distribution, oscillation
548 periods, and amplitude characteristics of NIOs, thereby demonstrating their
549 effectiveness and reliability in observing oceanic dynamical responses to
550 typhoons. This study provides high-quality observational data to support
551 further research into the mechanisms of typhoon-upper ocean interactions.

552 5 Data availability

553 The paired data for Typhoon-UGs/AUVs have been made publi
554 cly available along with this paper and can be accessed on Zenodo
555 via https://doi.org/10.5281/zenodo.19656867 (Qi et al., 2026). The ty
556 phoon best-track data (IBTrACS) were obtained from https://www.nc
557 ei.noaa.gov/products/international-best-track-archive. CMEMS Level-4
558 SLA data were obtained from https://data.marine.copernicus.eu. ERA
559 5 precipitation and evaporation data were obtained from https://cds.c
560 limate.copernicus.eu/datasets.

https://doi.org/10.5194/essd-2026-300
Preprint. Discussion started: 20 May 2026

6 Conclusions and outlook

Based on a six-month joint observation campaign involving both UGs and AUVs, this study has constructed a high-resolution, long-term dataset of ocean temperature and salinity profiles under typhoon conditions. This comprehensive dataset comprises 4459 profiles and covers seven typhoon events. A total of 62 UGs and 2 AUVs were deployed, yielding 112 sets of valid paired samples of typhoon event data and observations from UGs/AUVs. As the first long-term temperature and salinity dataset equipped with active observation devices, this study captures the evolution of typhoon-driven vertical structures of upper ocean temperature and salinity, as well as near-inertial oscillation signals. This dataset provides an observational foundation for studying the response processes of the upper ocean under typhoon forcing and reveals the complex nonlinear interaction mechanisms among wind-driven mixing, precipitation input, and background eddies. However, quantitative studies on the transfer of typhoon energy to the ocean and its transmission efficiency still require longer-term, more intensive observation data from UG and AUV.

In addition to moored buoys, we are pleased to note that UGs and AUVs have proven capable of capturing NIOs events, revealing the vertical structural characteristics of stratification changes. Although UG and AUV demonstrate unique advantages in capturing NIOs, their sampling methods still have certain limitations. Due to the use of zigzag

https://doi.org/10.5194/essd-2026-300
Preprint. Discussion started: 20 May 2026


Open Access Earth System Science Data Discussions

583 trajectories for spatial scanning, their horizontal movement speed is far
584 lower than the phase velocity of near-inertial waves, making them prone to
585 spatiotemporal aliasing effects when reconstructing the horizontal velocity
586 field. This spatial aliasing caused by the sampling trajectories may distort
587 high-frequency velocity signals, leading to a systematic underestimation of
588 near-inertial kinetic energy. Future plans include cross-validating and time-
589 constraining data using moored buoys or performing multi-profile phase
590 correction using repeated observations.

591 The main challenges encountered during observations include: (1)
592 partial data loss under extreme sea conditions; (2) some equipment failed
593 to effectively cover the target area due to the route deviating from the
594 typhoon's forced core region. Future optimizations can be made in the
595 following areas: (1) improving the buoyancy control system, enhancing the
596 wind and wave resistance of the equipment housing, and establishing a
597 real-time data quality monitoring and anomaly handling mechanism; (2)
598 prioritizing high-frequency sampling in the typhoon's near-field and forced
599 core region, while dynamically adjusting the observation route based on
600 typhoon track forecasts to capture rapid response processes in the upper
601 ocean. Resolving these issues will require continued collaboration among
602 the field operations team, platform engineers, and dynamical
603 oceanographers to drive further optimization of the autonomous sampling
604 system.

https://doi.org/10.5194/essd-2026-300
Preprint. Discussion started: 20 May 2026

Appendix A

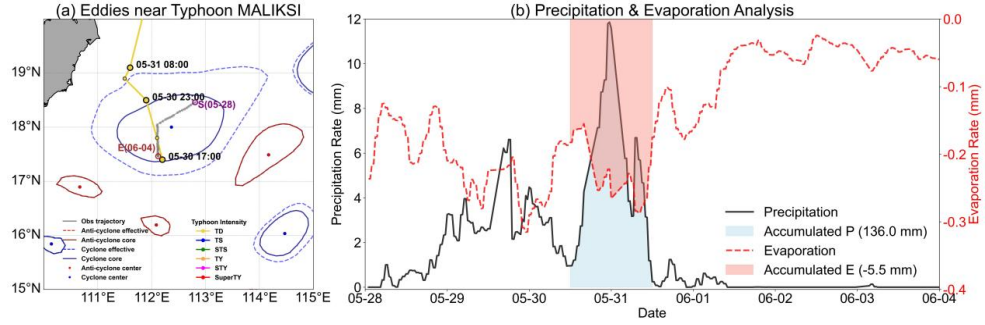

Figure A1. (a) Eddy distribution on May 31 and (b) precipitation and evaporation along the UG track during Typhoon MALIKSI (No. 2402). (a) shows that during MALIKSI passage, the UG track remained within a background cold eddy, which exhibited "low temperature and high salinity" characteristics. (b) shows that from May 30 to May 31 (when the UG was closest to the typhoon track), the 24 h cumulative precipitation and evaporation were 136 mm (reaching the level of a torrential rain event) and −5.5 mm, respectively. This resulted in a net freshwater flux of 141.5 mm, constituting an extreme precipitation event that would form a significant "freshwater cap" at the ocean surface, leading to a decrease in surface seawater salinity.

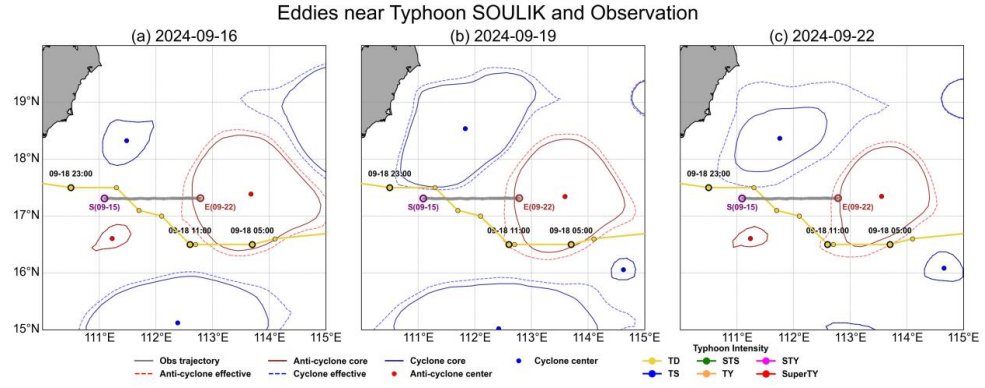

Figure A2 Distribution of eddies during Typhoon SOULIK (No. 2415) on (a) Sept. 16, (b) Sept. 19, and (c) Sept. 22, 2024. During this period, UG entered a background warm eddy. Its "high-temperature, low-salinity" characteristics caused a decrease in salinity in the temperature-salinity section, forming a nonlinear interaction process of "cooling and desalination" with the typhoon-induced cooling (Fig. 5B(b) and (c)).

https://doi.org/10.5194/essd-2026-300
Preprint. Discussion started: 20 May 2026

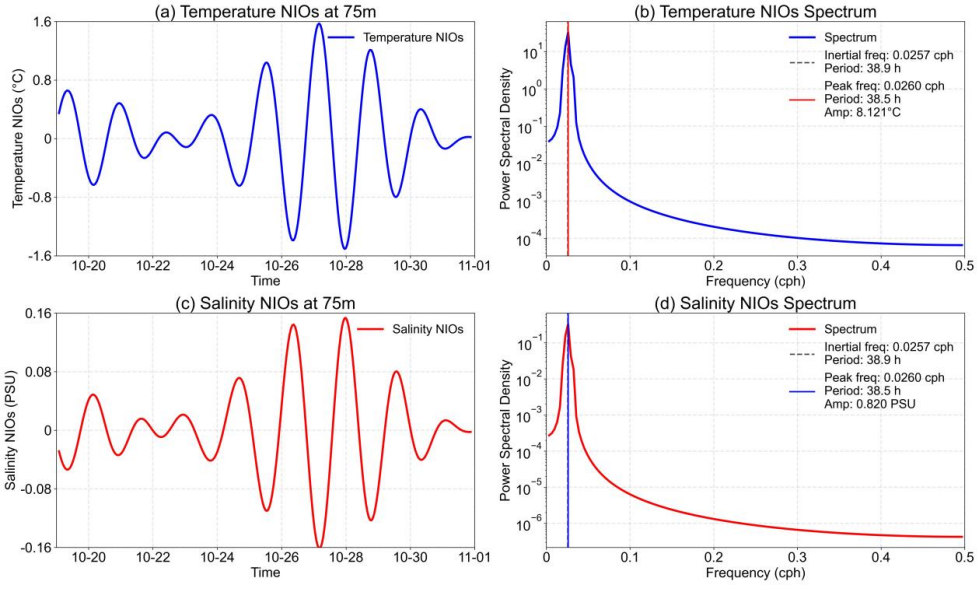

Figure A3. (a) Temperature NIOs and (b) salinity NIOs observed at a depth of 75 m during Typhoon TRAMI (No. 2420), along with (c) the power spectrum of the temperature NIOs and (d) the power spectrum of the salinity NIOs. The NIOs frequency calculated from the power spectra (0.0260 cph) deviates from the local inertial frequency (0.0257 cph) by only 1%, and the calculated oscillation period (38.5 h) deviates from the inertial period (38.9 h) by only 0.4 h, indicating that the NIOs oscillation period captured by the observation system is in excellent agreement with the local inertial period.

Author contributions

Conceptualization: Lei Liu, Jianfang Fei. Data curation: Jiawei Qi, Wenhu Liu. Investigation: Jiancheng Yu, Zhiduo Tan, Huabin Mao. Project administration: Zhanhong Ma, Xiaogang Huang, Xiaoping Cheng. Writing: Jiawei Qi, Lei Liu. All the authors have read and agreed to the published version of the paper.

Competing interests

https://doi.org/10.5194/essd-2026-300
Preprint. Discussion started: 20 May 2026

Open Access Earth System Science Data Discussions

638 The contact author has declared that none of the authors has any
639 competing interests.

640 Disclaimer

641 Publisher's note: Copernicus Publications remains neutral with regard
642 to jurisdictional claims made in the text, published maps, institutional
643 affiliations, or any other geographical representation in this paper. While
644 Copernicus Publications makes every effort to include appropriate place
645 names, the final responsibility lies with the authors.

646 Acknowledgements

647 We acknowledge all the colleagues and project members who have
648 contributed to the design of UGs and AUVs, the sea experiments, and data
649 processing in the past. Many scientists, engineers, and students have
650 participated in active surveys and mappings.

651 Financial support

652 This research received support by the National Natural Science
653 Foundation of China (grant no. 42192552), the National Natural Science
654 Foundation of China (grant no. 42330610) and the Key Project of the
655 Hunan Provincial Natural Science Foundation (grant no. 2025JJ30014).

https://doi.org/10.5194/essd-2026-300
Preprint. Discussion started: 20 May 2026

Reference

Athulya, K., Girishkumar, M. S., Aswathy, V. S., Sherin, V. R., Shivaprasad, S., Sureshkumar, N., and Rama Rao, E. P.: Near-Inertial Kinetic Energy and Diapycnal Heat Flux to the Mixed Layer During Tropical Cyclone *Bulbul* in the Northern Bay of Bengal Using High-Resolution Moored Buoy Observation, JGR Oceans, 131, e2025JC023384, https://doi.org/10.1029/2025JC023384, 2026.

Chen, H., Li, S., He, H., Song, J., Ling, Z., Cao, A., Zou, Z., and Qiao, W.: Observational study of super typhoon Meranti (2016) using satellite, surface drifter, Argo float and reanalysis data, Acta Oceanol. Sin., 40, 70–84, https://doi.org/10.1007/s13131-021-1702-9, 2021.

Chen, L., Zhang, X., Zhang, Z., and Zhang, W.: Mooring Observations of Typhoon Trami (2024)-Induced Upper-Ocean Variability: Diapycnal Mixing and Internal Wave Energy Characteristics, Remote Sensing, 17, 2604, https://doi.org/10.3390/rs17152604, 2025.

Chen, L., Zhang, Z., Jiang, Y., Zhang, X., Li, J., Zhang, W., and Wang, H.: Observation of Typhoon Trami (2024)-induced energy cascade from near-inertial waves to diurnal internal tides, Atmospheric and Oceanic Science Letters, 19, 100712, https://doi.org/10.1016/j.aosl.2025.100712, 2026.

Fan, K., Wang, X., Liu, J., and Shao, C.: Spatiotemporal Variability of Tropical Cyclone–Induced Ocean Heat Uptake and Its Effect on Ocean Heat Content, Journal of Climate, 36, 3481–3497, https://doi.org/10.1175/JCLI-D-22-0595.1, 2023.

Garau, B., Ruiz, S., Zhang, W. G., Pascual, A., Heslop, E., Kerfoot, J., and Tintoré, J.: Thermal Lag Correction on Slocum CTD Glider Data, Journal of Atmospheric and Oceanic Technology, 28, 1065–1071, https://doi.org/10.1175/JTECH-D-10-05030.1, 2011.

Gong, Y., Chen, L., Liu, M., Xu, J., Chen, Z., and Cai, S.: Three-Dimensional Characteristics and Dominant Forcing Mechanisms of Third Waves Generated by Nonlinear Near-Inertial Wave and Internal Tide Interactions, Geophysical Research Letters, 53, e2025GL120443, https://doi.org/10.1029/2025GL120443, 2026.

Goni, G., Todd, R., Jayne, S., Halliwell, G., Glenn, S., Dong, J., Curry, R., Domingues, R., Bringas, F., Centurioni, L., DiMarco, S., Miles, T., Morell, J., Pomales, L., Kim, H.-S., Robbins, P., Gawarkiewicz, G., Wilkin, J., Heiderich, J., Baltes, B., Cione, J., Seroka, G., Knee, K., and Sanabia, E.: Autonomous and Lagrangian Ocean Observations for Atlantic Tropical Cyclone Studies and Forecasts, Oceanog., 30, 92–103, https://doi.org/10.5670/oceanog.2017.227, 2017.

Guan, S., Jin, F.-F., Tian, J., Lin, I.-I., Pun, I.-F., Zhao, W., Huthnance, J., Xu, Z., Cai, W., Jing, Z., Zhou, L., Liu, P., Zhang, Y., Zhang, Z., Zhou, C., Yang, Q., Huang, X., Hou, Y., and Song, J.: Ocean internal tides suppress tropical cyclones in the South China Sea, Nat Commun, 15, 3903, https://doi.org/10.1038/s41467-024-48003-y, 2024.

https://doi.org/10.5194/essd-2026-300
Preprint. Discussion started: 20 May 2026

He, H., Tian, R., Lyu, X., Ling, Z., Sun, J., and Cao, A.: Annual Review of In Situ Observations of Tropical Cyclone–Ocean Interaction in the Western North Pacific during 2023, Remote Sensing, 16, 1990, https://doi.org/10.3390/rs16111990, 2024a.

He, H., Ling, Z., Wu, S., Lyu, X., Zeng, Z., Tian, R., Wang, Y., and Sun, J.: In situ observation of ocean response to tropical cyclone in the western North Pacific during 2022, Front. Mar. Sci., 11, 1445071, https://doi.org/10.3389/fmars.2024.1445071, 2024b.

Huang, Y.: Unveiling Hainan's Cutting-Edge Typhoon Defense Technology, Hainan Daily, A035th August, https://doi.org/10.28356/n.cnki.nhlrb.2025.006476, 2025.

John, E. B., Balaguru, K., Leung, L. R., Foltz, G. R., and Hagos, S. M.: Faster recovery of North Atlantic tropical cyclone-induced cold wakes in recent decades, npj Clim Atmos Sci, 8, 188, https://doi.org/10.1038/s41612-025-01029-5, 2025.

Li, H., Xu, F., and Wang, G.: Global Mapping of Mesoscale Eddy Vertical Tilt, JGR Oceans, 127, e2022JC019131, https://doi.org/10.1029/2022JC019131, 2022.

Li, J., Zhang, H., Liu, S., Wang, X., and Sun, L.: The Response and Feedback of Ocean Mesoscale Eddies to Four Sequential Typhoons in 2014 Based on Multiple Satellite Observations and Argo Floats, Remote Sensing, 13, 3805, https://doi.org/10.3390/rs13193805, 2021.

Liao X., Xu X., Huang X., and Sang K.: Modulation of the Kuroshio on Near-Inertial Internal Waves Induced by Typhoons Observed near the Luzon Strait, Periodical of Ocean University of China, 55, 13–24, https://doi.org/10.16441/j.cnki.hdxb.20230318, 2025.

Liu, Y., Weisberg, R. H., and Lembke, C.: Glider Salinity Correction for Unpumped CTD Sensors across a Sharp Thermocline, in: Coastal Ocean Observing Systems, Elsevier, 305–325, https://doi.org/10.1016/B978-0-12-802022-7.00017-1, 2015.

Liu, Y., Wan, Y., Cheng, Z., Isyaku, R., and Lü, H.: A case study on tropical cyclone Oma-induced phytoplankton bloom in eastern Australia, Journal of Marine Systems, 253, 104178, https://doi.org/10.1016/j.jmarsys.2025.104178, 2026.

Lu, Z., Liang, C., and Shang, X.: Main Component in Altimetry-Observed Response to a Tropical Cyclone, J. Phys. Oceanogr., 55, 75–93, https://doi.org/10.1175/JPO-D-24-0109.1, 2025.

Mei, W., Primeau, F., McWilliams, J. C., and Pasquero, C.: Sea surface height evidence for long-term warming effects of tropical cyclones on the ocean, Proc. Natl. Acad. Sci. U.S.A., 110, 15207–15210, https://doi.org/10.1073/pnas.1306753110, 2013.

Mishra, S., Parekh, A., Murali, K. R. P., and Chowdary, J. S.: Simulation of upper ocean temperature under the cyclone condition: a sensitivity to shape function in KPP mixing parameterisation, Ocean Dynamics, 76, 32, https://doi.org/10.1007/s10236-026-01781-z, 2026.

https://doi.org/10.5194/essd-2026-300
Preprint. Discussion started: 20 May 2026

729 Morison, J., Larson, N., D'asaro, E., and Boyd, T.: The Correction for Thermal-Lag Effects in
730 Sea-Bird CTD Data, Journal of Atmospheric & Oceanic Technology, 11,
731 https://doi.org/10.1175/1520-0426(1994)0112.0.CO;2, 1994.

732 Price, J. F.: Upper Ocean Response to a Hurricane, J. Phys. Oceanogr., 11, 153–175,
733 https://doi.org/10.1175/1520-0485(1981)011%253C0153:UORTAH%253E2.0.CO;2, 1981.

734 Qi, J., Liu, L., Liu, W., Fei, J., Yu, J., Ma, Z., Chen, Z., Mao, H., Tan, Z., Huang, X., and
735 Cheng, X.: High-resolution dataset of 2024 typhoons in the northern South China Sea (v3),
736 https://doi.org/10.5281/zenodo.19656867, 2026.

737 Qiu, C., Du, Z., Tang, H., Yi, Z., Qiao, J., Wang, D., Zhai, X., and Wang, W.: A high-
738 resolution temperature–salinity dataset observed by autonomous underwater vehicles for the
739 evolution of mesoscale eddies and associated submesoscale processes in the South China Sea,
740 Earth Syst. Sci. Data, 17, 3189–3202, https://doi.org/10.5194/essd-17-3189-2025, 2025.

741 Rainville, L., Lee, C. M., Arulananthan, K., Jinadasa, S. U. P., Fernando, H. J. S.,
742 Priyadarshani, W. N. C., and Wijesekera, H.: Water Mass Exchanges between the Bay of
743 Bengal and Arabian Sea from Multiyear Sampling with Autonomous Gliders, Journal of
744 Physical Oceanography, 52, 2377–2396, https://doi.org/10.1175/JPO-D-21-0279.1, 2022.

745 Reichl, B. G., Wittenberg, A. T., Griffies, S. M., and Adcroft, A.: Improved Equatorial Upper
746 Ocean Vertical Mixing in the NOAA/GFDL OM4 Model,
747 https://doi.org/10.22541/essoar.170785794.47537760/v1, 13 February 2024.

748 Ruan, Z., Li, B., Yu, C., Ding, R., Bai, P., and Wu, Q.: The impact of tropical cyclone outer
749 size on ocean surface responses, Front. Mar. Sci., 11, 1429384,
750 https://doi.org/10.3389/fmars.2024.1429384, 2024.

751 Sala, J., Giglio, D., Hu, A., Kuusela, M., Wood, K. M., and Lee, A. B.: Upper-ocean changes
752 with hurricane-strength wind events: a study using Argo profiles and an ocean reanalysis,
753 Ocean Sci., 20, 1441–1455, https://doi.org/10.5194/os-20-1441-2024, 2024.

754 Tang, H., Wang, D., Shu, Y., Yu, X., Shang, X., Qiu, C., Yu, J., and Chen, J.: Vigorous Forced
755 Submesoscale Instability Within an Anticyclonic Eddy During Tropical Cyclone "Haitang"
756 From Glider Array Observations, JGR Oceans, 130, e2024JC021396,
757 https://doi.org/10.1029/2024JC021396, 2025.

758 Tian, R. and He, H.: Ocean response to tropical cyclone in western North Pacific during 2021,
759 J. Phys.: Conf. Ser., 3007, 012010, https://doi.org/10.1088/1742-6596/3007/1/012010, 2025.

760 Todd, R. E. and Ren, A. S.: Warming and lateral shift of the Gulf Stream from in situ
761 observations since 2001, Nat. Clim. Chang., 13, 1348–1352, https://doi.org/10.1038/s41558-
762 023-01835-w, 2023.

763 Trenggono, M., Berlianty, D., Priyono, B., Wei, Z., Li, S., and Xu, T.: Impact of the Fujiwhara
764 effect from tropical cyclones Seroja and Odette on ocean dynamic in Southern Indonesia:

https://doi.org/10.5194/essd-2026-300
Preprint. Discussion started: 20 May 2026

765 Insights from argo data and model analysis, Regional Studies in Marine Science, 80, 103877,
766 https://doi.org/10.1016/j.rsma.2024.103877, 2024.

767 Vlasova, G. A., Nguyen, X. B., Le, M. D., and Marchenko, S. S.: Influence of Tropical
768 Cyclones of the South China Sea on the Variability of the Vietnamese Coastal Current
769 Structure, Oceanology, 62, 13–21, https://doi.org/10.1134/S0001437022010180, 2022.

770 Wada, A. and Yanase, W.: Is the Increasing Trend in the Environmental Upper-Ocean Heat
771 Content in the Northwest Pacific Strengthening Tropical Cyclone Intensity?, in: Advances in
772 Hurricane Risk in a Changing Climate, vol. 3, edited by: Collins, J., Done, J., Zhu, Y.-J., and
773 Wilson, P., Springer Nature Switzerland, Cham, 97–124, https://doi.org/10.1007/978-3-031-
774 63186-3_5, 2024.

775 Wang, G., Wu, L., Mei, W., and Xie, S.-P.: Ocean currents show global intensification of
776 weak tropical cyclones, Nature, 611, 496–500, https://doi.org/10.1038/s41586-022-05326-4,
777 2022.

778 Wang, T., Zhang, S., Chen, F., Ma, Y., Jiang, C., and Yu, J.: Influence of sequential tropical
779 cyclones on phytoplankton blooms in the northwestern South China Sea, J. Ocean. Limnol.,
780 39, 14–25, https://doi.org/10.1007/s00343-020-9266-7, 2021.

781 Yang, B., Hu, P., and Hou, Y.: Observed Near-Inertial Waves in the Northern South China
782 Sea, Remote Sensing, 13, 3223, https://doi.org/10.3390/rs13163223, 2021.

783 Yang, L., Luo, X., Chen, S., Zhou, X.-L., Wang, W.-Q., and Wang, D.-X.: Characteristics of
784 rapidly intensifying tropical cyclones in the South China Sea, 1980–2016, Advances in
785 Climate Change Research, 13, 333–343, https://doi.org/10.1016/j.accre.2022.04.004, 2022.

786 Yang, Y. J., Yang, C.-Y., Jan, S., Chang, M.-H., Wei, C.-L., and Her, W.-H.: Advanced Moored
787 Data Buoys for Catching Typhoons in the Western North Pacific, mar technol soc j, 58, 52–
788 62, https://doi.org/10.4031/MTSJ.58.1.1, 2024.

789 Ye, H., Ma, Z., Fei, J., and Duan, Y.: Evaluation of Leftward Biased Cold Wakes Induced by
790 Tropical Cyclones in the North Hemisphere, JGR Oceans, 128, e2023JC020188,
791 https://doi.org/10.1029/2023JC020188, 2023.

792 Yi, Z., Qiu, C., Wang, D., Cai, Z., Yu, J., and Shi, J.: Submesoscale Kinetic Energy Induced
793 by Vertical Buoyancy Fluxes During the Tropical Cyclone Haitang, JGR Oceans, 129,
794 e2023JC020494, https://doi.org/10.1029/2023JC020494, 2024.

795 Yu, J., Zhang, A., Jin, W., Chen, Q., Tian, Y., and Liu, C.: Development and experiments of
796 the Sea-Wing underwater glider, China Ocean Eng, 25, 721–736,
797 https://doi.org/10.1007/s13344-011-0058-x, 2011.

798 Yu, L., Sun, J., Hui, Z., Xiong, X., Jin, S., Wang, L., Yang, G., Guo, Y., Ju, X., Chen, L., Hu,
799 X., and Li, Y.: The Ocean Heat Content Changes in the South China Sea due to Tropical
800 Cyclones with Different Tracks, Pure Appl. Geophys., 178, 269–286,

https://doi.org/10.5194/essd-2026-300
Preprint. Discussion started: 20 May 2026

https://doi.org/10.1007/s00024-020-02630-w, 2021.

Zhang, B., Wen, L., Perrie, W., and Kudryavtsev, V.: Sea Surface Height Response to Tropical Cyclone From Satellite Altimeter Observations and SAR Estimates, IEEE Trans. Geosci. Remote Sensing, 62, 1–9, https://doi.org/10.1109/TGRS.2024.3371168, 2024a.

Zhang, H.: Modulation of Upper Ocean Vertical Temperature Structure and Heat Content by a Fast-Moving Tropical Cyclone, Journal of Physical Oceanography, 53, 493–508, https://doi.org/10.1175/JPO-D-22-0132.1, 2023.

Zhang, H., Chen, D., Zhou, L., Liu, X., Ding, T., and Zhou, B.: Upper ocean response to typhoon Kalmaegi (2014), JGR Oceans, 121, 6520–6535, https://doi.org/10.1002/2016JC012064, 2016.

Zhang, H., He, H., Zhang, W.-Z., and Tian, D.: Upper ocean response to tropical cyclones: a review, Geosci. Lett., 8, 1, https://doi.org/10.1186/s40562-020-00170-8, 2021.

Zhang, H., Tian, D., Sun, Y., Yang, M., Yang, S., Zhou, Y., Sun, X., and Chen, D.: Unmanned vehicles probed inner-core air-sea conditions during Super Typhoon Koinu (2023), Science Bulletin, 69, 3789–3792, https://doi.org/10.1016/j.scib.2024.10.018, 2024b.

Zhang, Z., Qiu, B., Tian, J., Zhao, W., and Huang, X.: Latitude-dependent finescale turbulent shear generations in the Pacific tropical-extratropical upper ocean, Nat Commun, 9, 4086, https://doi.org/10.1038/s41467-018-06260-8, 2018.

Zheng, M. and Wang, C.: Interdecadal changes of tropical cyclone intensity in the South China Sea, Clim Dyn, 60, 409–425, https://doi.org/10.1007/s00382-022-06305-1, 2023.

Zhou, Y., Shan, K., and Lin, Y.: Shrinking cold wakes accelerate tropical cyclone intensification in recent decades, npj Clim Atmos Sci, 9, 25, https://doi.org/10.1038/s41612-025-01300-9, 2025.